2019 2nd IEEE International Conference on Soft Robotics (RoboSoft)
COEX, Seoul, Korea, April 14-18, 2019

Multi-Material Soft Strain Sensors with High Gauge Factors for Proprioceptive Sensing of Soft Bending Actuators

Myungsun Park[1], Yunsik Ohm[2], DongWook Kim[1], and Yong-Lae Park[1]

***Abstract*— Highly stretchable strain sensors, with embedded microchannels filled with conductive liquid, have been widely used in various applications in soft robotics for detecting different types of deformation modes, when attached to human or robot bodies. One of recent applications that draws an attention is direct integration of soft sensors with soft actuators for proprioceptive feedback. However, it is not easy to obtain a high resolution in curvature sensing when combined with bending actuators in which curvature is indirectly measured from strain sensing, since the placement of soft sensors are limited to the location where the strain sensitivity is relatively small. Therefore, we propose a new design of high gauge factor strain sensors using a multi-material structure. By alternately arranging low and high stiffness elastomers, the structure experiences amplified strain changes on each of the low-stiffness regions. The gauge factor was significantly increased as high as over three times of a conventional single material sensor. In this paper, the design and fabrication of the proposed sensor are described with an analytical model. The sensor was tested while integrated with a PneuNet bending actuator for curvature detection as an application.**

I. Introduction

The sensing mechanism of a soft actuation system must be studied along with the development of target soft robots. Soft bodied systems with soft actuators work in a variety of applications including biomimetic robots [1],[2], rehabilitation devices [3], and soft grippers [4]. For control, implementing a proper sensing mechanism inside the soft system is a key requirement. Thus, there have been approaches that measure deformation of flexible structures using different mechanisms, such as optical and magnetic sensing. However, each of these approaches has limitation in producing a fully soft system [5], detecting large deformation [6], or diversifying materials for the substrates [7]. Especially, embedding electronics in highly flexible and stretchable elastomeric substrates has been a challenging issue in many applications. Researchers have suggested special structures that allow unstretchable electronics to be embedded in soft substrates, such as arranging a stiff platform of electronic circuits in a compliant pattern [8], inducing buckling mechanics to produce a wavy shape of the metal which endures both stretch and shrinkage [9], [10].

Meanwhile, many researchers have tried to employ soft sensors embedded with microchannels and conductive liquid, such as room-temperature liquid metal (e.g. eutectic gallium-indium (EGaIn) and Galinstan) [11], [12] and room-temperature ionic liquid [13] for detecting deformation of soft system [14], [15]. The microfluidic sensing mechanism has an advantage of holding a large deformation without fracture while it is not imposing a constraint on the host material. Therefore, this type of soft sensors has been implemented in a number of applications, such as soft artificial skin [16] and muscles [17], wearable devices and robots [18] and soft grippers [19] since the early age of soft robotics.

For a soft bending actuator, the curvature of the actuator can be estimated by measuring the strain change above its neutral axis using the relationship of $\Delta\epsilon = d\Delta\kappa$, where $\Delta\epsilon, d$ and $\Delta\kappa$ are the strain change, the distance from the neutral axis, and the curvature change, respectively [15]. For sensitive measurement, the sensor must be placed as far away as possible from the neutral axis of the bending motion, which maximizes the strain change. Certain types of bending actuators, such as fiber-embedded actuators [20] allow the sensor to be placed on the top surface [19] where the strain becomes the highest during bending.

However, for PneuNet-type bending actuators, the sensor layer needs to be placed under the air chambers due to the separation of the chambers, which makes it difficult to have sufficient distance d for sensitivity. Although it is possible to produce a thicker bottom layer, it not only increases the form factor of the actuator but also degrades the actuation performance by constraining the deformation with increased bending stiffness. To address this issue, a sensor of high enough sensitivity is in demand with which a small form factor of the actuator can be achieved.

Therefore, we propose a new design of soft strain sensors with high gauge factors that can be easily embedded in the bottom layer of PneuNet-type actuators while maintaining a small form factor. The proposed sensor is composed of multiple elastomer segments with two different stiffnesses. This unique structure creates nonuniform strains in the segments and significantly increases strain changes in the low-stiffness region. Thus, uneven strain distribution is generated along the sensor, which consequently amplifies the gauge factor. In other words, selective strain concentration on the microchannel is made by the physical deformation of the sensor structure. This concept is similar to but distinguished

*This work was supported in part by the National Research Foundation of Korea (NRF) funded by the Korean Government (MSIT) under Grants NRF-2016R1A5A1938472 and NRF-2018M3C1B8017699, and in part by Technology Innovation Program (No.2017-10069072) funded by the Ministry of Trade, Industry & Energy (MOTIE), Korea. (Corresponding author: Yong-Lae Park)

[1]M. Park, D. Kim, and Y.-L. Park are with the Department of Mechanical and Aerospace Engineering, the Institute of Advanced Machines and Design (IAMD), and the Soft Robotics Research Center (SRRC), Seoul National University, Seoul, 08826, Korea. (E-mails: {arielrbts; shigumchis; ylpark}@snu.ac.kr)

[2]Y. Ohm is with the Department of Mechanical Engineering, Carnegie Mellon University, Pittsburgh, PA 15213, USA. (E-mail: yohm@andrew.cmu.edu)

Authorized licensed use limited to: Univ of Calif San Diego. Downloaded on February 01,2026 at 19:21:18 UTC from IEEE Xplore. Restrictions apply.

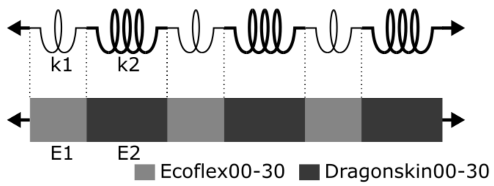

Fig. 1: Silicone segments of different stiffnesses connected in series. When each segment is modeled as a spring with its own stiffness, the total assembly can be considered as a series of springs.

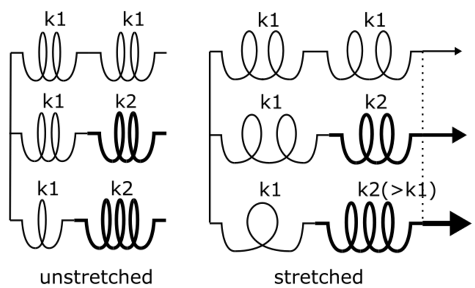

Fig. 2: Three sets of springs in series. Their stiffness distribution and initial lengths affect the final deformation. The softer and/or shorter spring stretches more.

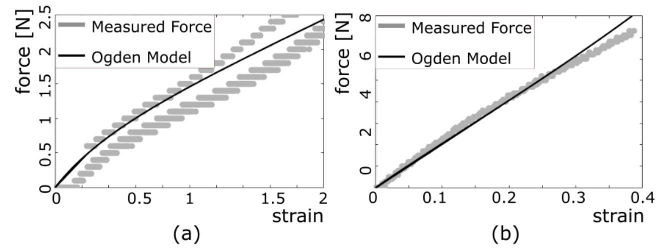

Fig. 3: Material characterization with Ogden nonlinear stress-strain relationship. (a) Ecoflex 00-30 ($\mu_1 = 2.06 \cdot 10^4$, $\mu_2 = 1.14 \cdot 10^4$). (b) Dragon Skin 30 ($\mu_1 = 9.88 \cdot 10^4$, $\mu_2 = 4.94 \cdot 10^4$).

from the structures which isolate the strain of the stiffer sensing material from its host substrate [8], [9], [10], in that our approach amplifies the strain of the sensing material while previous approaches use stiff sensing materials placed in the area of less strain concentration.

Furthermore, since the length ratio of the two materials is considered as a design parameter that affects the magnitude of the gauge factor, it is easy to control the gauge factor during the fabrication stage in our design. Finding how the parameter changes the sensitivity is important for achieving a desired sensor response. Even though similar work has suggested controlling the sensor response by changing the channel geometry [21] or dimensions [22], which makes fabrication complex and more expensive, the design of this work has its own contribution in that it does not directly manipulate the sensing medium, microchannels.

In this paper, the proposed sensor and its microchannel are first modeled. Then, the experimental results are compared with the prediction of the modeling, and the performance of the sensor is discussed with respect to its sensitivity and mechanical properties. Considering these characteristics, the PneuNet-type bending actuator is suggested as one of applications of the sensor. Several experiments with the actuator induce further discussion on how the multi-material high gauge factor strain sensor can be utilized and improved.

II. MODELING

According to previous studies, the strain response of microfluidic soft sensors are nonlinear in general [16], which is not desirable for accurate sensing. However, we take advantage of this characteristic to increase the strain sensitivity in this research. A long microfludic resistive channel is considered as a set of finite numbers of small segments connected in series, embedded in a silicone substrate. Then, the total resistance of the sensor can be calculated as the sum of those of all the microchannel segments. When we model each silicone segment as a spring (Figure 1), the deformation of the entire springs is determined by their stiffness distribution and the initial length (Figure 2). When the stiffness through the length is distributed, softer part stretches more. The initial length of the distributed-stiffness segments also affects the shape of deformation. With this simple spring analogy, we expect that we can control the strain distribution of the sensor by designing the stiffness and the initial length of the silicone substrate. By controlling the strain distribution, the total resistance change of the sensor, which is calculated using a nonlinear strain-resistance relationship, can be controlled as well. In this section, this design concept is verified with mathematical modeling.

A. Material Characterization: Ogden Model

We used Ecoflex 00-30 (Smooth-On, Inc.) as the soft material and Dragon Skin 30 (Smooth-On, Inc.) as the stiff material, which are expressed as the two springs of different stiffness in Figures 1 and 2. The elastic modulus of the stiff material is 8.6 times larger than the soft material. The length ratio of the two materials is considered as a design parameter, which determines the sensor characteristic as the final result. To verify the result, the deformation of each segment in Figure 1 should be determined first. The Ogden model for nonlinear elastic material relates strain ϵ or stretch $\lambda\ (= \epsilon+1)$ to the force P under uni-axial tension.

$$P = \mu_1 A_0(\lambda - \frac{1}{\lambda^2}) + \mu_2 A_0(\lambda^3 - \frac{1}{\lambda^3}) \qquad (1)$$

where $\mu_1 + 2\mu_2 = E/3$, and A_0 is the cross-sectional area. The two materials were modeled by fitting the equation (1) to its experimental result with μ_1 and μ_2 (Figure 3). 100% modulus of silicone provided from the manufacturer was used as the elastic modulus for the Ogden model.

B. Strain: Force Equilibrium on Each Segment

When the silicone segments connected in series are stretched, the cross-sectional force through the length is

Authorized licensed use limited to: Univ of Calif San Diego. Downloaded on February 01,2026 at 19:21:18 UTC from IEEE Xplore. Restrictions apply.

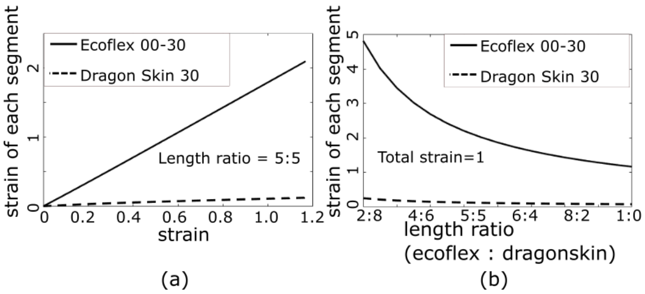

Fig. 4: Calculated strain of each segment. (a) Due to the constant tensile force through the length, soft material experiences larger stretch. (b) When total strain is fixed (=1), the length ratio of the segments affects the strain distribution. As the portion of the soft material decreases, strains on both segments increases.

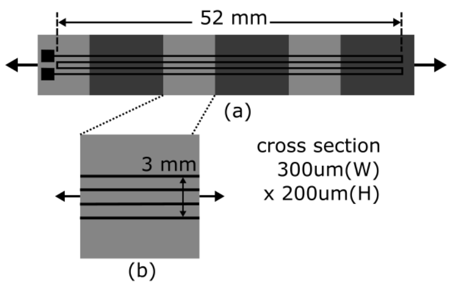

Fig. 5: (a) Microchannel design. The entire microchannel in (a) can be considered as a set of small microchannels on a segment in (b).

constant, so

$$
\begin{aligned}
P &= \mu_{e,1} A_0 (\lambda_e - \frac{1}{\lambda_e^2}) + \mu_{e,2} A_0 (\lambda_e^3 - \frac{1}{\lambda_e^3}) \\
&= \mu_{d,1} A_0 (\lambda_d - \frac{1}{\lambda_d^2}) + \mu_{d,2} A_0 (\lambda_d^3 - \frac{1}{\lambda_d^3})
\end{aligned} \tag{2}
$$

Stretches for each material have another relation given the total length L.

$$L_{e,0}\lambda_e + L_{d,0}\lambda_d = L \tag{3}$$

Solving equations (2) and (3) simultaneously provides the strain distribution through the silicone substrate, λ_e and λ_d, as a function of total strain,

$$\epsilon = \frac{L}{L_{d,0} + L_{e,0}} - 1 \tag{4}$$

Figure 4(a) predicts the strain of each segment when the length ratio of the two materials is fixed (1:1), as a function of the total strain. The softer material deforms more and faster than the stiffer material. Figure 4(b) plots the strain of each segment by varying the length ratio and fixing the total strain. As the portion of soft material becomes smaller, the strain of the soft material rapidly increases.

C. Total Resistance: Microchannel Characterization

Figure 5(a) describes the sensor design including the microchannel. The EGaIn microchannel is embedded in the silicone substrate whose strain distribution is calculated in Section II. *B*. The microchannel embedded in each segment (Figure 5(b)) is deformed following the strain of the substrate. Since the segments are connected in series, the total

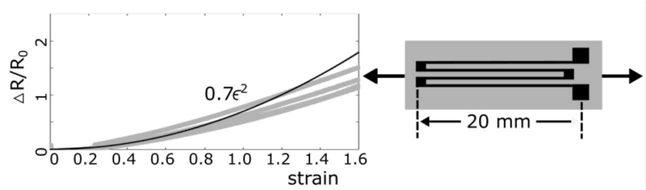

Fig. 6: Piezoresistive microchannel characterization with test sample design. Change of resistance due to strain and its polynomial fitting.

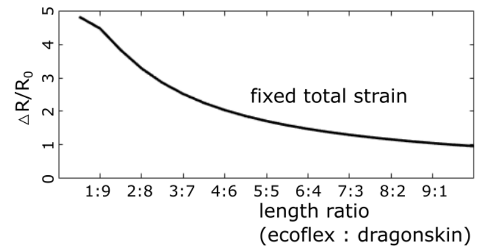

Fig. 7: Total resistance prediction. As the portion of the material becomes smaller, the magnitude of the total resistance change becomes larger.

resistance of the microchannel is the sum of the resistances of the segments,

$$R(\epsilon) = \sum_i R_i(\epsilon_i) \tag{5}$$

where i represents each segment. For each segment, the resistance change (ΔR_i) divided by the initial resistance (R_{i0}) is a function of the strain (ϵ_i).

$$\frac{\Delta R_i}{R_{i0}} = \frac{\Delta R_i}{R_{i0}}(\epsilon_i) \tag{6}$$

Then, the total resistance change divided by the initial resistance can be calculated as a function of the strains ϵ_i of each segment.

$$\frac{\Delta R}{R_0}(\epsilon) = \frac{1}{R_0} \sum_i \left\{ \frac{\Delta R_i}{R_{i0}}(\epsilon_i) \cdot R_{i0} \right\} \tag{7}$$

Therefore, the strain-resistance relationship of the segments in equation (6) have to be found to obtain the total strain-resistance relationship. To experimentally find the relationship, the test microchannel embedded in Ecoflex 00-30 (Figure 6, right) was fabricated, having an identical cross-sectional dimension with the original sensor in Figure 5. By stretching the microchannel, the relationship was experimentally found (Figure 6, left).

Using this resistance-strain relationship and the strains of the segments calculated in Section II. *B*, the resistance of each segment can be calculated, and then the total resistance by equation (7) can be calculated. The less portion of the soft material (Ecoflex 00-30) means the larger total resistance, as shown in Figure 7. The next section verifies this result experimentally.

III. Design and Fabrication

A. Sensor Design

As a way to implement our model into the soft strain sensor, Ecoflex 00-30 and Dragon skin 30 of different

Authorized licensed use limited to: Univ of Calif San Diego. Downloaded on February 01,2026 at 19:21:18 UTC from IEEE Xplore. Restrictions apply.

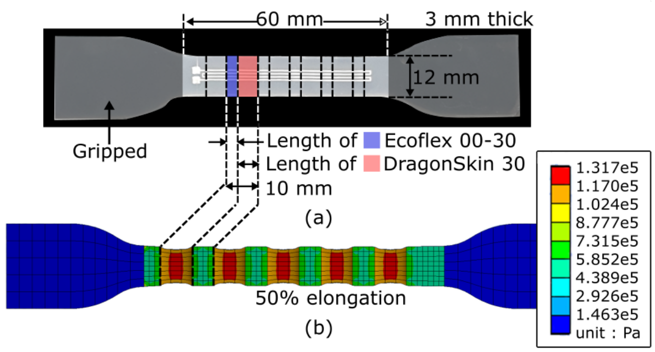

Fig. 8: (a) Sensor prototype with dimensions. (b) FEA result for predicting the behavior of multiple segments with different stiffness with 50% elongation.

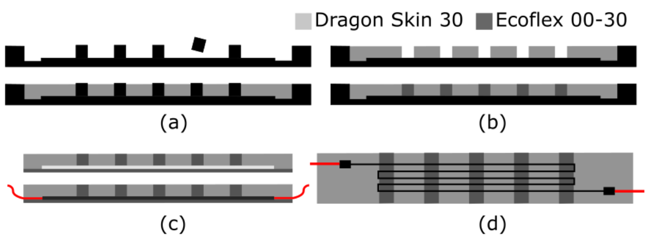

Fig. 9: Fabrication of strain sensor. (a) Assembly of small blocks with the mold and pouring of Dragon Skin 30. (b) Casting Ecoflex 00-30. (c) Sealing the microchannel with spin-coated layer and filling with EGaIn. (d) Top view of the sensor.

stiffness were alternately placed in which the microchannel of Figure 5 was embedded (Figure 8(a)). The finite element analysis (FEA) result (Figure 8(b)) using a commercial software package (ANSYS) shows that the softer material stretches more than the harder material under tensile force. We parameterize the length of each material and figure out how the length ratio affects the total resistance change.

B. Fabrication

The soft sensor was fabricated using multiple pieces of 3D-printed rigid plastic molds, as shown in Figure 9. First, multiple small blocks are assembled in a microchannel-patterned mold, and liquid-state Dragon Skin 30 is poured into the mold (Figure 9(a)). Once Dragon Skin cures, the small blocks are removed and the spaces from the blocks are filled with liquid-state Ecoflex 00-30 (Figure 9(b)). While curing, the two silicone elastomers easily bond. A single piece of silicone containing two different materials with the microchannel pattern on the bottom is extracted from the mold. The microchannel is then sealed with a thin Ecoflex layer spin coated at 100 rpm for 50 seconds. EGaIn is finally injected into the microchannel and the signal wires are connected (Figure 9(c-d)).

C. Experimental Setup

Figure 10(a-e) shows five different test samples that are unstretched and stretched in the tensile test. Each sample has different length ratio of the soft and the stiff materials. The experimental setup is shown in Figure 10(f). The sensor signal and the force and the strain data were collected. The

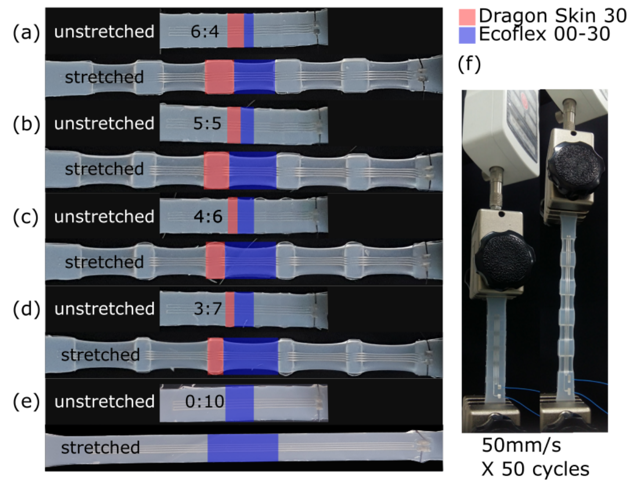

Fig. 10: (a-e) Test samples (stretched/unstretched) of different length ratios of the materials. As the ratio varies, the shape of deformation changes. (f) Experimental setup for the tensile test. The samples were stretched and released 50 cycles repeated at 5 mm/sec.

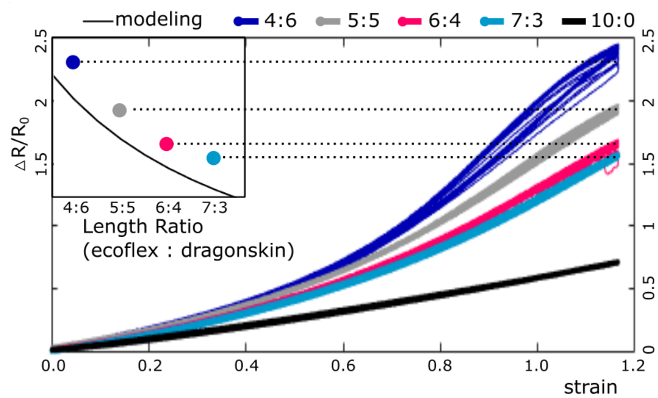

Fig. 11: Sensor characterization plot for five different prototypes compared with model and conventional strain sensor. Data of 50 cycles each. The top left figure plots the sensor signal of the test samples when the total strain is constant (=1.16).

sensors were stretched and released repeatedly (50 times) at 5 mm/s.

IV. Results

A. Tensile Test

1) Sensor Characterization: Figure 11 is the result of the tensile test with the five test samples in Figure 10. Each curve indicates superimposed signals of the 50 repetitions, showing highly repeatable. When comparing the single-material strain sensor (ecoflex:dragonskin=10:0, black curve) to the multi-material strain sensors, we found that the sensors using multiple materials of different stiffness have much higher sensitivity. The top-left part of the plot compares the modeling result of Figure 7 (fixed total strain of 1.16) and the experimental data points.Although the model prediction and the experimental result have an agreement in trend, the model underestimated the magnitude of the results. The difference came from two major inaccuracies in the model: the parameters of the Ogden stress-strain relationship in Figure 3 and the

Authorized licensed use limited to: Univ of Calif San Diego. Downloaded on February 01,2026 at 19:21:18 UTC from IEEE Xplore. Restrictions apply.

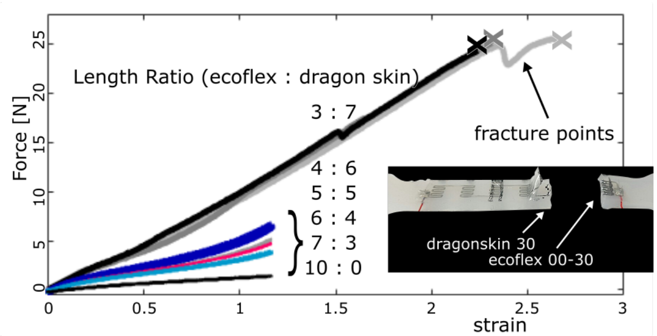

Fig. 12: Fracture analysis. Additional sample of length ratio of 3:7, which experiences larger tensile force under same strain, was made for conservative fracture analysis. The sample failed at strains between 2 and 2.5 at the boundary of the materials.

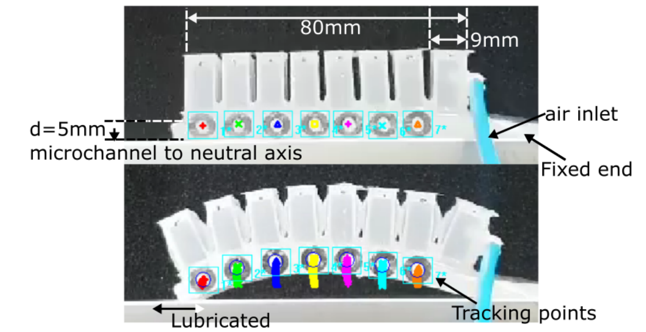

Fig. 13: PneuNet-type actuator prototype and experimental setup. The actuator was placed on a horizontal flat surface with lubricated contact. Curvature was calculated by tracking the points on the base line with motion analysis software.

resistance-strain relationship of the microchannel in Figure 6, which are both determined experimentally. Especially, the fact that the microchannel of the test sample in Figure 6 is not identical to the microchannel in the real prototype (Figure 5(b)) leaves room for the model to be further improved in the future.

2) Fracture Analysis: In general, a multi-material structure is more likely to fail at the boundary of the materials due to stress concentration. Figure 12 plots the tensile force during stretching. When we fixed the total strain, and as the soft material occupied less, the strain on the segments became larger (Figure 4(b)) and the force to stretch became larger. The most conservative design is to find the fracture point of the samples with the least soft material. An additional sample with the length ratio of 3:7 was manufactured for the fracture analysis. The sample experienced fracture on the boundary of the materials at strains between 2 and 2.5.

V. Application: Curvature Estimation for Soft Bending Actuator

In this section, embedding the proposed soft strain sensor in a PneuNet-type bending actuator is suggested for taking advantage of its high sensitivity. In this case, the sensor needs to be placed at the bottom of the actuator so the sensor does not constrain the expansion of separate air chambers of the actuator. The strain during bending is calculated from the curvature κ as

$$\Delta\epsilon = d\Delta\kappa \tag{8}$$

The bending stiffness of the actuation system increases when d becomes larger, which requires large input pressure. To avoid this, d should be smaller while sacrificing $\Delta\epsilon$. Therefore, a sensor with a high sensitivity is necessary for detecting the small range of strain changes.

A. Design, Fabrication and Experimental Setup

Figure 13 describes the design of the actuator prototype and the experimental setup. Two identical actuators were manufactured by embedding a single and a multi-material sensor layers, respectively, to validate the efficacy of the proposed sensor. The distance d from the neutral axis to the microchannel was 5 mm for both cases. The actuators with

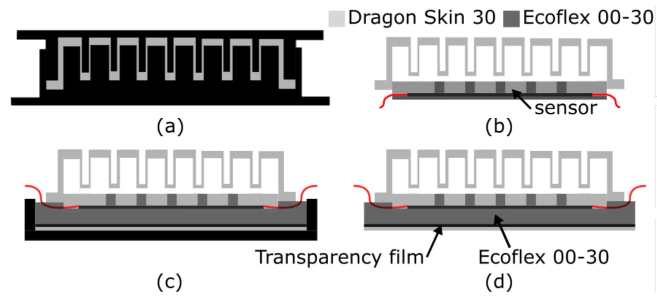

Fig. 14: Fabrication of PneuNet actuator embedded with strain sensor. (a) Dragon Skin 30 is cast in the mold leaving space for the sensor. (b) Strain sensor attached on the bottom of the actuator with Dragon Skin 30. (c-d) The assembly immersed on the top of base material, Ecoflex 00-30, and transparency film.

a sensor were placed on the ground with one end fixed and the other end free to move with lubrication. While giving input air pressure the deformations of the actuators were video-recorded and tracked using a motion analysis software package (ProAnalyst) to calculate the curvature.

Figure 14 shows the fabrication method of the sensor-integrated PneuNet actuator. Dragon Skin 30 is cast while leaving the space for the sensor to be embedded (Figure 14(a)). The sensor is embedded in the actuator (Figure 14(b)) and the assembly is immersed in a mold on the bottom of which transparency film and base of Ecoflex 00-30 is placed (Figure 14(c-d)).

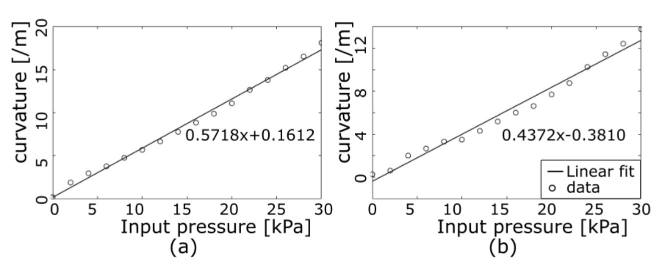

Fig. 15: Input pressure-curvature characterization for the two actuators. (a) single material sensor embedded. (b) multi-material sensor embedded.

Authorized licensed use limited to: Univ of Calif San Diego. Downloaded on February 01,2026 at 19:21:18 UTC from IEEE Xplore. Restrictions apply.

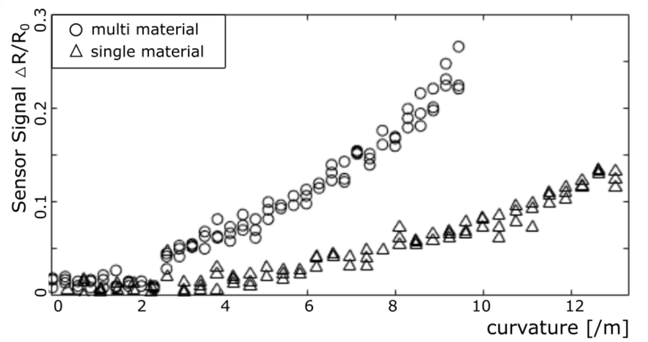

Fig. 16: Curvature of the actuator to sensor output signal. The pressure input was given to the system, and curvature of each point was calculated using the linear fit in Figure 15. The actuator with multi-material sensor showed larger sensitivity.

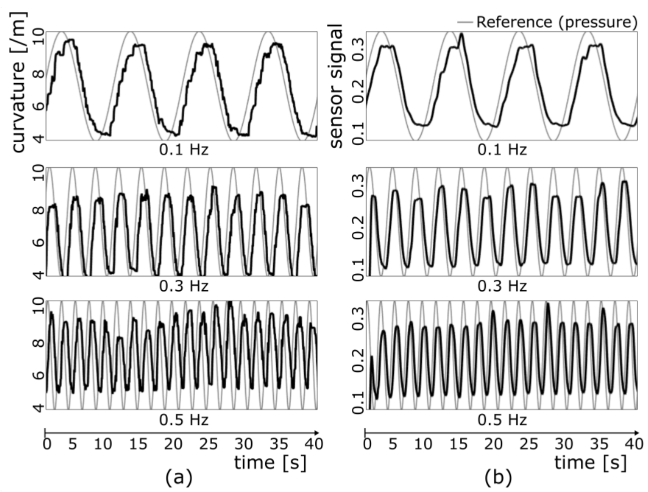

Fig. 17: Actuator curvature (a) and sensor signal (b) under dynamic loading of 0.1/0.3/0.5 Hz sinusoidal inputs. Both of the curvature and the sensor signal follow the input well. The delay is due to the regulator delay.

B. Characterization

Figures 15 and 16 show the results of the actuator characterization. The deformation of the actuator was characterized by giving discrete input pressures from 0 to 30 kPa and calculating the curvature. The relationship between the pressure and the curvature was linearly fitted in Figure 15. In Figure 16, each point indicates the curvature of the moment, which was calculated from the input pressure using the relationship in Figure 15, and the sensor signal. The sensor signal is non-linear to the curvature $\Delta\kappa = \Delta\epsilon/d \propto \Delta\epsilon$, which can be predicted from Figure 12. When comparing the two sensors, the multi-material sensor was more sensitive to the curvature change. This means that the multi-material sensor can better detect the deformation of the actuator than the single-material sensor given the measurement system of identical resolution.

C. Dynamic Response

Figure 17 plots the curvature (a) and the sensor signal (b) of the actuation system while given the sinusoidal pressure input. The delays in both results are from the delay of the regulator, not from the actuator or the sensor itself. We found that the deformations (curvature) followed the

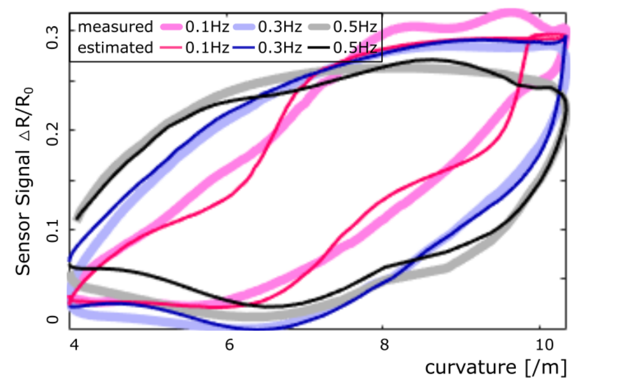

Fig. 18: Hysteresis analysis under dynamic loading frequencies of 0.1 Hz (pink), 0.3 Hz (blue), 0.5 Hz (black). The light-colored curves indicate the output data of experiment and the curves with solid lines show the estimation of hysteresis loops.

dynamic inputs and the sensor output was able to detect the deformation well.

D. Hysteresis

The elasomer material of the PneuNet actuator experiences hysteresis due to the viscoelastic effect and the characteristic of the pneumatic system. The hysteresis can be characterized using logic operators or deep-learning approaches [23], [24]. Here, the hysteresis of the actuator was analyzed with the Preisach operator. The experimental data was transformed into Preisach domain using the equation below.

$$y = \int\int_{a \geq b} \mu(\beta,\alpha) R(\beta,\alpha)[\mu,\xi] d\beta d\alpha \quad (9)$$

$$F(\alpha,\beta) = \int\int_{T} R(\alpha,\beta)\mu(\beta,\alpha) d\beta d\alpha \quad (10)$$

Here, α and β are Preisach domain variables, μ is the weight in each location of Preisach domain, and *R* is a relay function.

Figure 18 demonstrates the hysteresis analysis of the sensor output under the dynamic inputs of different frequencies in Figure 17. The magnitude of the hysteresis became larger as the frequency of the input signal increased. With the Preisach model, each of the hysteresis curve was estimated well, which implies the possibility of the dynamic control using the proposed actuation system.

VI. Discussion and Future Work

In this research, we proposed the design of high gauge factor soft strain sensors using a multi-material structure, of which we can control the sensitivity by changing the length ratio. We then suggested the PneuNet-type actuator as an example of applications of the proposed sensor. Considering the geometry of the PneuNet actuator particularly, it is advantageous to reduce its thickness, which makes the range of strain changes smaller however. Therefore, our high sensitive strain sensor is appropriate for sensing small deformation.

However, as the portion of the soft material becomes even smaller, the strains on the soft segments become larger, which results in large tensile force during stretching. Sensors with

Authorized licensed use limited to: Univ of Calif San Diego. Downloaded on February 01,2026 at 19:21:18 UTC from IEEE Xplore. Restrictions apply.

a high modulus is not desirable not only for its own failure but also for the fact that it can constrain the behavior of the host system. Therefore, the trade-off of the multi-material structure between the sensitivity and the rigidity should be compromised by determining the optimal length ratio for further applications as suggested in previous study [25].

In addition, the proposed structure has drawbacks of complex fabrication and stress concentration at the material boundary. This issue can be addressed by introducing a new fabrication techniques, such as bonding of two materials without an adhesive agent, direct printing of liquid elastomers in uncured states, or implementing stiffness gradient boundaries.

VII. Conclusion

A method of designing high gauge factor soft strain sensors using a multi-material structure was proposed in this work. We modeled the structure using the stress-strain relationship of nonlinear solids and the resistance-strain relationship of the microchannel. Then, the proposed method was experimentally validated using actual prototypes, which revealed the amplification of the gauge factor and the effect of the length ratio on the gauge factor. We also showed the possibility of the sensor to be embedded in an actual system with an example application of PneuNet type bending actuator.

References

[1] K. Suzumori, S. Endo, T. Kanda, N. Kato, and H. Suzuki, “A bending pneumatic rubber actuator realizing soft-bodied manta swimming robot,” in *Robotics and Automation, 2007 IEEE International Conference on*. IEEE, 2007, pp. 4975–4980.

[2] A. D. Marchese, C. D. Onal, and D. Rus, “Autonomous soft robotic fish capable of escape maneuvers using fluidic elastomer actuators,” *Soft Robotics*, vol. 1, no. 1, pp. 75–87, 2014.

[3] P. Polygerinos, Z. Wang, K. C. Galloway, R. J. Wood, and C. J. Walsh, “Soft robotic glove for combined assistance and at-home rehabilitation,” *Robotics and Autonomous Systems*, vol. 73, pp. 135–143, 2015.

[4] R. Deimel and O. Brock, “A novel type of compliant and underactuated robotic hand for dexterous grasping,” *The International Journal of Robotics Research*, vol. 35, no. 1-3, pp. 161–185, 2016.

[5] S. Ozel, N. A. Keskin, D. Khea, and C. D. Onal, “A precise embedded curvature sensor module for soft-bodied robots,” *Sensors and Actuators A: Physical*, vol. 236, pp. 349–356, 2015.

[6] Y.-L. Park, S. Elayaperumal, B. Daniel, S. C. Ryu, M. Shin, J. Savall, R. J. Black, B. Moslehi, and M. R. Cutkosky, “Real-time estimation of 3-d needle shape and deflection for mri-guided interventions,” *IEEE/ASME Transactions On Mechatronics*, vol. 15, no. 6, pp. 906–915, 2010.

[7] C. To, T. L. Hellebrekers, and Y.-L. Park, “Highly stretchable optical sensors for pressure, strain, and curvature measurement,” in *Intelligent Robots and Systems (IROS), 2015 IEEE/RSJ International Conference on*. IEEE, 2015, pp. 5898–5903.

[8] T. Li, Z. Suo, S. P. Lacour, and S. Wagner, “Compliant thin film patterns of stiff materials as platforms for stretchable electronics,” *Journal of materials research*, vol. 20, no. 12, pp. 3274–3277, 2005.

[9] A. Volynskii, S. Bazhenov, O. Lebedeva, and N. Bakeev, “Mechanical buckling instability of thin coatings deposited on soft polymer substrates,” *Journal of materials science*, vol. 35, no. 3, pp. 547–554, 2000.

[10] H. Jiang, D.-Y. Khang, J. Song, Y. Sun, Y. Huang, and J. A. Rogers, “Finite deformation mechanics in buckled thin films on compliant supports,” *Proceedings of the National Academy of Sciences*, vol. 104, no. 40, pp. 15 607–15 612, 2007.

[11] Y.-L. Park, C. Majidi, R. Kramer, P. Bérard, and R. J. Wood, “Hyperelastic pressure sensing with a liquid-embedded elastomer,” *Journal of Micromechanics and Microengineering*, vol. 20, no. 12, p. 125029, 2010.

[12] M. D. Dickey, R. C. Chiechi, R. J. Larsen, E. A. Weiss, D. A. Weitz, and G. M. Whitesides, “Eutectic gallium-indium (egain): a liquid metal alloy for the formation of stable structures in microchannels at room temperature,” *Advanced Functional Materials*, vol. 18, no. 7, pp. 1097–1104, 2008.

[13] D. Y. Choi, M. H. Kim, Y. S. Oh, S.-H. Jung, J. H. Jung, H. J. Sung, H. W. Lee, and H. M. Lee, “Highly stretchable, hysteresis-free ionic liquid-based strain sensor for precise human motion monitoring,” *ACS applied materials & interfaces*, vol. 9, no. 2, pp. 1770–1780, 2017.

[14] T. Giffney, M. Xie, A. Yong, A. Wong, P. Mousset, A. McDaid, and K. Aw, “Soft pneumatic bending actuator with integrated carbon nanotube displacement sensor,” *Robotics*, vol. 5, no. 1, p. 7, 2016.

[15] A. Koivikko, E. S. Raei, M. Mosallaei, M. Mäntysalo, and V. Sariola, “Screen-printed curvature sensors for soft robots,” *IEEE Sensors Journal*, vol. 18, no. 1, pp. 223–230, 2018.

[16] Y.-L. Park, B.-R. Chen, and R. J. Wood, “Design and fabrication of soft artificial skin using embedded microchannels and liquid conductors,” *IEEE Sensors Journal*, vol. 12, no. 8, pp. 2711–2718, 2012.

[17] J. P. King, L. E. Valle, N. Pol, and Y.-L. Park, “Design, modeling, and control of pneumatic artificial muscles with integrated soft sensing,” in *Robotics and Automation (ICRA), 2017 IEEE International Conference on*. IEEE, 2017, pp. 4985–4990.

[18] J.-B. Chossat, Y. Tao, V. Duchaine, and Y.-L. Park, “Wearable soft artificial skin for hand motion detection with embedded microfluidic strain sensing,” in *Robotics and Automation (ICRA), 2015 IEEE International Conference on*. IEEE, 2015, pp. 2568–2573.

[19] J. Morrow, H.-S. Shin, C. Phillips-Grafflin, S.-H. Jang, J. Torrey, R. Larkins, S. Dang, Y.-L. Park, and D. Berenson, “Improving soft pneumatic actuator fingers through integration of soft sensors, position and force control, and rigid fingernails.” in *ICRA*, 2016, pp. 5024–5031.

[20] P. Polygerinos, Z. Wang, J. T. Overvelde, K. C. Galloway, R. J. Wood, K. Bertoldi, and C. J. Walsh, “Modeling of soft fiber-reinforced bending actuators,” *IEEE Transactions on Robotics*, vol. 31, no. 3, pp. 778–789, 2015.

[21] Y.-L. Park, D. Tepayotl-Ramirez, R. J. Wood, and C. Majidi, “Influence of cross-sectional geometry on the sensitivity and hysteresis of liquid-phase electronic pressure sensors,” *Applied Physics Letters*, vol. 101, no. 19, p. 191904, 2012.

[22] D. M. Vogt, Y.-L. Park, and R. J. Wood, “Design and characterization of a soft multi-axis force sensor using embedded microfluidic channels,” *IEEE Sensors Journal*, vol. 13, no. 10, pp. 4056–4064, 2013.

[23] D. Kim and Y.-L. Park, “Contact localization and force estimation of soft tactile sensors using artificial intelligence,” in *2018 IEEE/RSJ International Conference on Intelligent Robots and Systems (IROS)*. IEEE, 2018, pp. 7480–7485.

[24] S. Han, T. Kim, D. Kim, Y.-L. Park, and S. Jo, “Use of deep learning for characterization of microfluidic soft sensors,” *IEEE Robotics and Automation Letters*, vol. 3, no. 2, pp. 873–880, 2018.

[25] J. Wirekoh and Y.-L. Park, “Design of flat pneumatic artificial muscles,” *Smart Materials and Structures*, vol. 26, no. 3, p. 035009, 2017.

Authorized licensed use limited to: Univ of Calif San Diego. Downloaded on February 01,2026 at 19:21:18 UTC from IEEE Xplore. Restrictions apply.